# Power Balance Optimization of Cascaded H-Bridge Multilevel Converters for Large-Scale Photovoltaic Integration

Yifan Yu, *Student Member, IEEE*, Georgios Konstantinou, *Member, IEEE*, Branislav Hredzak, *Senior Member, IEEE*,
and Vassilios G. Agelidis, *Senior Member, IEEE*

***Abstract*—Multilevel-cascaded H-bridge converters are promising candidates for next generation photovoltaic power converters. They feature reduced switching losses and higher conversion efficiency with modular structure; characteristics vital for large-scale photovoltaic power plants. However, the stochastically-variable nature of irradiance levels and ambient temperatures affects the normal operation of this topology, because power levels in the three phases can be unequal. The existing zero sequence injection method can deal with the power imbalance problem, but it is limited in its application. The paper proposes a zero sequence injection method to optimize the converter power balance, extending the converter operation with severe power imbalance. Based on the proposed optimal method, a simplified optimal zero sequence injection method requiring less calculation effort is derived and compared with the optimal method. Simulation and experimental results validate the effectiveness and feasibility of the proposed methods.**

***Index Terms*—AC–DC power converters, cascaded H-bridge converter, multilevel converter, photovoltaics.**

## NOMENCLATURE

| | |
|---|---|
| $\mathbf{V_{ga}}, \mathbf{V_{gb}}, \mathbf{V_{gc}}$ | Three-phase grid voltage vectors. |
| $v_{ga}, v_{gb}, v_{gc}$ | Three-phase grid voltages (instantaneous values). |
| $V_g$ | Grid voltage (line-to-line) (rms). |
| $\mathbf{V_a}, \mathbf{V_b}, \mathbf{V_c}$ | Three-phase converter output voltage vectors. |
| $v_a, v_b, v_c$ | Three-phase converter output voltages (instantaneous values). |
| $\mathbf{V_{La}}, \mathbf{V_{Lb}}, \mathbf{V_{Lc}}$ | Three-phase inductor voltage vectors. |
| $\mathbf{V^0}$ | Fundamental frequency zero sequence vector. |
| $v^0$ | Zero sequence (instantaneous value). |
| $v_f^0$ | Fundamental frequency zero sequence component of the optimal zero sequence injection (instantaneous value). |
| $V^0$ | Fundamental frequency zero sequence component (rms). |
| $\mathbf{V^{0'}}$ | Fundamental frequency vector of the simplified optimal zero sequence injection. |
| $\mathbf{V^{0*}}$ | Error vector between $\mathbf{V^0}$ and $\mathbf{V^{0'}}$. |
| $v_{\mathrm{dc}}$ | Capacitor (dc side) voltage of H-bridges. |
| $V_p$ | Magnitude of the square wave of the optimal zero sequence injection. |
| $V_p^{'}$ | Magnitude of the square wave of the simplified optimal zero sequence injection. |
| $\mathbf{I_{ga}}, \mathbf{I_{gb}}, \mathbf{I_{gc}}$ | Three-phase grid current vectors. |
| $i_{ga}, i_{gb}, i_{gc}$ | Three-phase grid currents (instantaneous values). |
| $I_g$ | Grid current (rms). |
| $\square^+$ | Positive sequence. |
| $\square^-$ | Negative sequence. |
| $H$ | Unit capacitance constant. |
| $L_f$ | Three-phase filtering inductors. |
| $P_{\mathrm{nom}}$ | Three-phase nominal power (peak). |
| $p_{a,b,c}$ | Instantaneous power generated in phases $a$, $b$, $c$. |
| $\alpha$ | Phase angle between converter output voltage vectors and grid current vectors. |
| $\beta$ | Positive-to-negative zero-crossing angle of the optimal zero sequence injection. |
| $\gamma$ | Positive-to-negative zero-crossing angle of the fundamental frequency zero sequence injection. |
| $\delta$ | Phase angle between the negative sequence grid current vector (phase $a$) and the positive sequence grid current vector (phase $a$). |
| $\eta$ | Three-phase current (voltage) imbalance factor. |
| $\theta$ | Phase angle of fundamental frequency zero sequence component. |
| $\theta'$ | Phase angle of fundamental frequency zero sequence component of the simplified zero sequence injection. |
| $\lambda_a, \lambda_b, \lambda_c$ | Three-phase power generation ratios. |
| $\bar{\lambda}$ | Average three-phase power generation ratio. |
| $\omega$ | Angular frequency. |

## I. INTRODUCTION

MULTILEVEL power converters have been attracting attention from researchers worldwide because of their outstanding characteristics [1]–[6]. Their multilevel waveform synthesis allows switches to operate with lower frequency, thus

---

Manuscript received November 5, 2014; revised January 8, 2015; accepted February 20, 2015. Date of publication February 27, 2015; date of current version September 29, 2015. Recommended for publication by Associate Editor H. Li.

The authors are with the Australian Energy Research Institute and the School of Electrical Engineering and Telecommunications, University of New South Wales, Sydney, 2052 NSW, Australia (e-mail: yifan.yu@student.unsw.edu.au; g.konstantinou@unsw.edu.au; b.hredzak@unsw.edu.au; vassilios.agelidis@unsw.edu.au).

Color versions of one or more of the figures in this paper are available online at http://ieeexplore.ieee.org.

Digital Object Identifier 10.1109/TPEL.2015.2407884

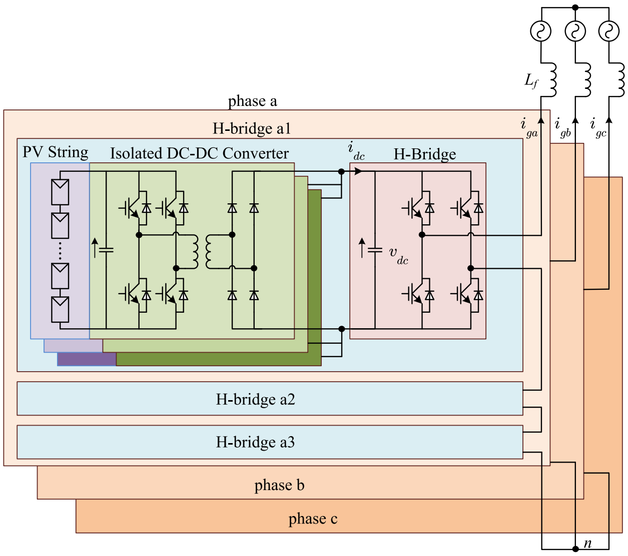

Fig. 1. Three-phase seven-level CHB converter.

resulting in reduced switching losses and higher conversion efficiency. Also, medium voltage levels can be easily reached with low voltage switching devices, which are readily available in the market.

Among all practical multilevel topologies, the cascaded H-bridge (CHB) multilevel converter is considered as one of the most suitable configurations for large-scale photovoltaic (PV) power plants [7]–[19]. When the topology is used in high power motor drives, one of the drawbacks is the presence of multiple independent dc links, because a set of bulky transformers is usually needed to provide isolated dc sources [2], [20]. However, this problem does not exist in PV applications, because the multiple dc links can be readily connected to separate PV strings.

Fig. 1 shows the three-phase, seven-level CHB converter investigated in this paper. The converter consists of nine H-bridges, each fed by multiple PV strings via separate dc–dc converters. A high-frequency isolation transformer is mandatory in the dc–dc converter to isolate the PV modules from the grid, because most commercial PV modules can withstand no more than 1000 V between the active part and the grounded frame [21]. The transformer also helps increase the voltage gain of the dc–dc converter, so that maximum power point tracking (MPPT) can still be achieved under low irradiance levels. The dc side capacitor voltages $v_{\mathrm{dc}}$ are regulated by the voltage-oriented control (VOC), while each dc–dc converter conducts independent MPPT to maximize the captured power. The arrangement has two more attractive features. The modular structure first allows easy extension to reach higher voltage and power levels, thus making it feasible to connect the whole PV farm to the medium voltage network with a single converter. In addition, the bulky and heavy line-frequency power transformers are no longer necessary, since galvanic isolation has been provided by embedded compact high-frequency transformers.

The CHB converter was initially designed with each H-bridge generating an equal amount of power. However, in PV applications, the power generated by the PV modules connected to each bridge can be unequal, because of nonuniform solar irradiance, unequal ambient temperatures, partial shading and/or inconsistent module degradation. This power imbalance problem can be classified into two categories [17], [18]: 1) interphase (clustered) power imbalance, which occurs when each phase generates a different amount of power; and 2) interbridge (individual) power imbalance, which happens when each bridge in the same phase leg generates a different amount of power. The objective of the power balance control is to deliver three-phase balanced currents to the grid, with unequal PV power generation in each bridge.

Since the interphase and interbridge power imbalance can be addressed using independent controllers, this paper focuses on the interphase power imbalance. One way to solve the interphase power imbalance of three-phase CHB converters is to inject a zero sequence component into the converter output voltages [15]–[18]. A fundamental frequency zero sequence injection (FFZSI) that redistributes the generated power among the three phases has been derived through instantaneous power theory [15] and phasor diagrams [16], respectively. The injection of the zero sequence increases the required converter output voltages, which are usually limited by the dc-side voltages. Once the limit is reached, the converter saturates and three-phase balanced grid currents cannot be provided. FFZSI exploits the relatively low dc-side voltages in such an inefficient way that the voltage limit is easily reached with a slight power imbalance.

To deal with severe power imbalance, this paper proposes an optimal zero sequence injection (OZSI). The method fully exploits the voltage overhead provided by the converter, and is able to achieve three-phase balanced grid currents in the case of severe power imbalance, where conventional FFZSI fails. Based on the preliminary concept discussed in [22], this paper provides a detailed derivation of the proposed method with a thorough analysis and extensive experimental verification. An additional simplified optimal zero sequence injection (SOZSI) is proposed in the paper. Compared with OZSI, the simplified method features reduced calculation effort by avoiding numerical iterations, but introduces additional negative sequence grid currents.

The rest of the paper is organized as follows. The conventional FFZSI and the relation between the fundamental frequency component of the zero sequence injection and power rebalance are reviewed in Section II. The concept, derivation and discussions of OZSI are covered in Section III. In Section IV, SOZSI is derived and evaluated as an alternative to OZSI. Simulation results of a 10-MW PV power plant and experimental results from a scaled-down prototype (9 kW) are provided in Sections V and VI, respectively, to validate the effectiveness and feasibility of the presented methods. In Section VII, the final conclusions are drawn.

## II. Review of Conventional Method

Fig. 2 shows the phasor diagram for balanced power generation. $\mathbf{V_{ga}}$, $\mathbf{V_{gb}}$, $\mathbf{V_{gc}}$ and $\mathbf{I_{ga}}$, $\mathbf{I_{gb}}$, $\mathbf{I_{gc}}$ represent the grid voltage and current vectors, respectively, while $\mathbf{V_a}$, $\mathbf{V_b}$, $\mathbf{V_c}$ represent the converter output voltage vectors. Fig. 3 demonstrates how the three-phase grid currents become asymmetrical,

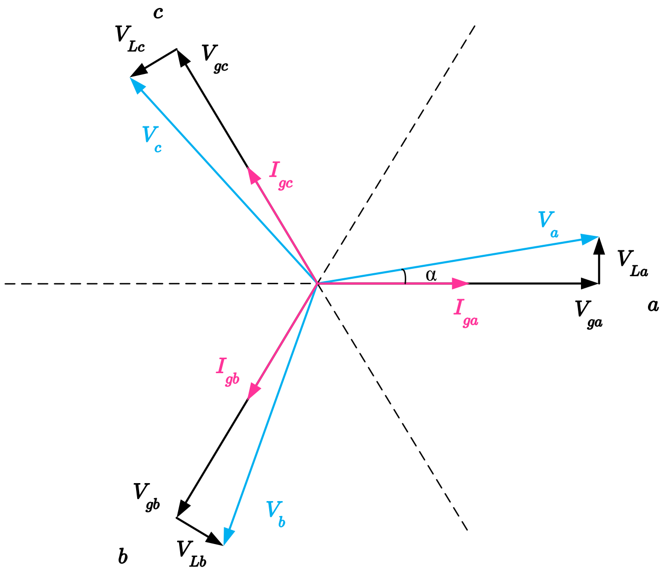

Fig. 2. Phasor diagram for balanced operation of a CHB converter.

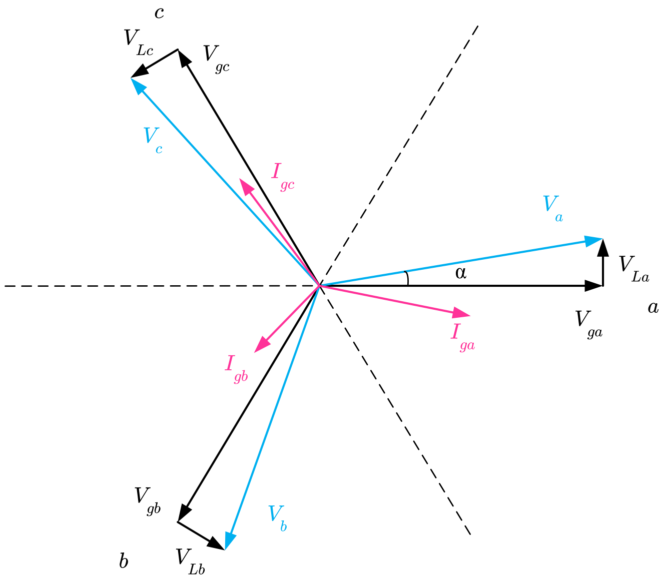

Fig. 3. Phasor diagram for unbalanced operation of a CHB converter.

when the interphase power imbalance occurs and the converter output voltages are left unchanged.

An indicator of the interphase power imbalance is given by the power generation ratios $\lambda_a$, $\lambda_b$ and $\lambda_c$

$$\lambda_{a,b,c} = \frac{p_{a,b,c}}{P_{\mathrm{nom}}/3} \tag{1}$$

which compares the actual generated power of each phase to the single-phase nominal power $P_{\mathrm{nom}}/3$. The injection of a fundamental frequency zero sequence component into the converter output voltages is able to rebalance the three-phase grid currents [15], [16]. The power redistribution among the three phases by the injected zero sequence vector $\mathbf{V^0}$ and the grid current vectors $\mathbf{I_{ga}}, \mathbf{I_{gb}}, \mathbf{I_{gc}}$ (see Fig. 4) can be expressed as

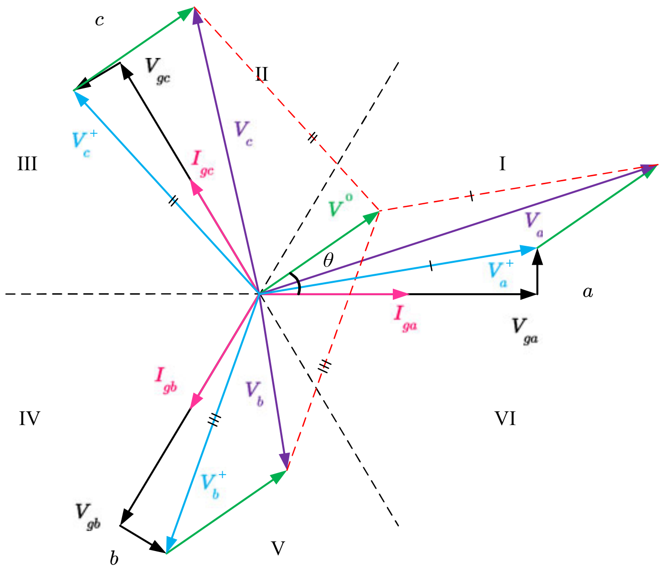

Fig. 4. Phasor diagram for unbalanced operation with FFZSI.

$$V^0 I_g \cos\theta = \Delta P_a = (\lambda_a - \bar{\lambda})\,\frac{P_{\mathrm{nom}}}{3} \tag{2a}$$

$$V^0 I_g \cos(\theta + 2\pi/3) = \Delta P_b = (\lambda_b - \bar{\lambda})\,\frac{P_{\mathrm{nom}}}{3} \tag{2b}$$

$$V^0 I_g \cos(\theta - 2\pi/3) = \Delta P_c = (\lambda_c - \bar{\lambda})\,\frac{P_{\mathrm{nom}}}{3} \tag{2c}$$

$$\bar{\lambda} = \frac{\lambda_a + \lambda_b + \lambda_c}{3}. \tag{2d}$$

The FFZSI can thus be derived as

$$v^0 = \sqrt{2} V^0 \cos(\omega t + \theta) \tag{3}$$

where

$$V^0 = \frac{\sqrt{6}\Delta}{3(\lambda_a + \lambda_b + \lambda_c)} V_g \tag{4a}$$

$$\theta = \begin{cases} \sin^{-1}\left(\dfrac{\sqrt{6}\,(\lambda_c - \lambda_b)}{2\Delta}\right) & \text{Sectors (I), (VI)} \\ \dfrac{2\pi}{3} + \sin^{-1}\left(\dfrac{\sqrt{6}\,(\lambda_b - \lambda_a)}{2\Delta}\right) & \text{Sectors (II), (III)} \\ \dfrac{4\pi}{3} + \sin^{-1}\left(\dfrac{\sqrt{6}\,(\lambda_a - \lambda_c)}{2\Delta}\right) & \text{Sectors (IV), (V)} \end{cases} \tag{4b}$$

$$\Delta = \sqrt{(\lambda_a - \lambda_b)^2 + (\lambda_b - \lambda_c)^2 + (\lambda_a - \lambda_c)^2} \tag{4c}$$

and the sector can be determined via Table I.

Eq. (4) shows that the rms value $V^0$ of the FFZSI is expected to increase with the severity of the power imbalance. Injection of the zero sequence into the positive sequence increases the maximum converter output voltages, which are, on the other hand,

TABLE I
LOCATION OF ZERO SEQUENCE VECTOR $\mathbf{V}^0$

| Three-Phase Power Generation Ratios | Sector |
|---|---|
| $\lambda_b < \lambda_c < \lambda_a$ | (I) |
| $\lambda_b < \lambda_a < \lambda_c$ | (II) |
| $\lambda_a < \lambda_b < \lambda_c$ | (III) |
| $\lambda_a < \lambda_c < \lambda_b$ | (IV) |
| $\lambda_c < \lambda_a < \lambda_b$ | (V) |
| $\lambda_c < \lambda_b < \lambda_a$ | (VI) |

constrained by the dc-side voltages. If the required converter output voltages fall within the limit set by the dc-side voltages, FFZSI is able to deliver balanced grid currents even with unbalanced power generation. However, when the power imbalance among the three phases increases, the required converter output voltages are likely to exceed the limit and overmodulation occurs. Methods that better exploit the limited converter output voltages are necessary to extend the effective range of power balance control.

## III. OZSI

The fundamental frequency component of the zero sequence redistributes power among the three phases, by generating unequal amounts of power with three-phase grid currents (see Fig. 4). The harmonic component of the zero sequence, on the other hand, should not affect the power redistribution and can be modified arbitrarily, since it does not generate any active power with the grid currents. Therefore, the optimal solution should satisfy two requirements: 1) its fundamental frequency component should be equal to FFZSI; and 2) its harmonic component should make the converter output voltage peak as low as possible.

### *A. Concept*

Since it is challenging to find the harmonic component required to make the converter output voltage peak as low as possible, this paper approaches the problem from a different perspective. We first try to investigate, based on a certain converter output voltage peak, $V_p$, how to generate the zero sequence with the largest possible fundamental frequency component. Then by equating the obtained fundamental frequency component to the FFZSI of (3) and (4), the required converter output voltage peak $V_p$ can be solved. Finally, by subtracting the positive sequence from the converter output voltages with the peak value $V_p$, the proposed OZSI is obtained.

Fig. 5(a) shows the positive sequence component of the converter output voltages $v_a^+$, $v_b^+$ and $v_c^+$ and the injected zero sequence $v^0$ with FFZSI. $v_a^+$, $v_b^+$ and $v_c^+$ lead three-phase grid currents $i_{ga}$, $i_{gb}$ and $i_{gc}$, respectively, by $\alpha$, owing to the filtering inductor $L_f$ shown in Fig. 1. The converter output voltages are expected to reach beyond the limitation set by the dc link capacitor voltage, which, in this case, is $3v_{\mathrm{dc}}$ [see Fig. 5(b)]. As a result, overmodulation occurs and three-phase balanced grid currents can no longer be achieved.

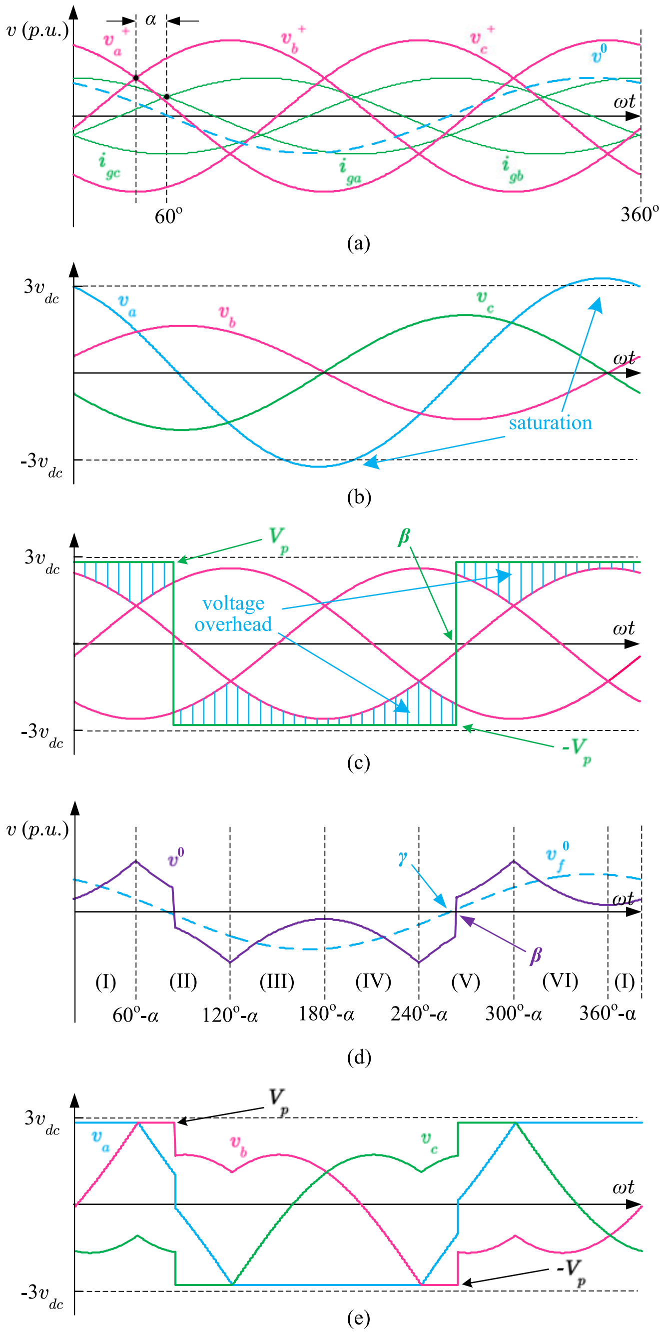

Fig. 5. OZSI. (a) Positive sequence component of the converter output voltages $v_a^+$, $v_b^+$ and $v_c^+$, the zero sequence injection $v^0$ with FFZSI, three-phase grid currents $i_{ga}$, $i_{gb}$ and $i_{gc}$; (b) Three-phase converter output voltages $v_a$, $v_b$ and $v_c$ with FFZSI; (c) Square wave and the voltage overhead; (d) OZSI $v^0$ and its fundamental frequency component $v_f^0$, (e) three-phase converter output voltages $v_a$, $v_b$ and $v_c$ with OZSI.

For a given converter output peak voltage $V_p$, the maximum voltage overhead, illustrated as the shaded area in Fig. 5(c), can only be achieved by forcing the external envelope of the converter output voltages to equal the square wave with an amplitude of $V_p$. If this voltage overhead is used as the injected zero sequence, its integral over a half period is maximized, which, as a result, means the largest fundamental frequency component. OZSI can then be obtained by subtracting the positive sequence from the square wave as shown in Fig. 5(d), with its fundamental frequency component $v_f^0$ equal to the zero sequence injection $v^0$ with FFZSI in Fig. 5(a).

The three-phase converter output voltages are plotted in Fig. 5(e), in which the converter output peak voltage $V_p$ rotates among the three phases. The sinusoidal waveforms of the converter output voltages with FFZSI in Fig. 5(b) are well below the limit for most of the time, but reach beyond the limit at the top. However, the presented OZSI makes full use of the voltage overhead available, and thus avoids the unwanted overmodulation with the same fundamental frequency component.

Since $V_p$ is usually lower than $3v_{\mathrm{dc}}$ [see Fig. 5(e)], all devices in the phase with its phase voltage equal to $V_p$ or $-V_p$ keep switching with a constant duty cycle. It is thus different from the discontinuous modulation which clamps the phase leg to a nonswitching state. The only exception is when the power imbalance increases to the critical point, and $V_p$ is equal to $3v_{\mathrm{dc}}$.

## B. Derivation

In Fig. 5(c) the duty cycle of the square wave with a peak voltage of $V_p$ should be $1/2$. Otherwise, the integral of the voltage overhead would not sum to zero, and a dc component would be introduced. The square wave is thus determined by the peak voltage $V_p$ and the zero-crossing angle (negative to positive) $\beta$, shown in Fig. 5(c). The presented OZSI can then be expressed by subtracting the positive sequence from the square wave in a piecewise manner as

$$v^0 = \begin{cases} V_p - v_a^+, & 0 \le \omega t < 60^\circ - \alpha \\ V_p - v_b^+, & 60^\circ - \alpha \le \omega t < \beta - \pi \\ -V_p - v_c^+, & \beta - \pi \le \omega t < 120^\circ - \alpha \\ -V_p - v_a^+, & 120^\circ - \alpha \le \omega t < 240^\circ - \alpha \\ -V_p - v_b^+, & 240^\circ - \alpha \le \omega t < \beta \\ V_p - v_c^+, & \beta \le \omega t < 300^\circ - \alpha \\ V_p - v_a^+, & 300^\circ - \alpha \le \omega t < 360^\circ \end{cases} \tag{5}$$

where $\alpha$ denotes the phase shift between the converter output voltages and grid voltages [see Figs. 2 and 5(a)]. The Fourier series of $v^0$ is given by

$$v^0 = \sum_{n=1}^{\infty} \left(a_n \cos n\omega t + b_n \sin n\omega t\right) \tag{6}$$

where

$$a_n = \frac{1}{\pi} \int_{-\pi}^{\pi} v^0 \cos n\omega t \, \mathrm{d}\omega t \tag{7}$$

$$b_n = \frac{1}{\pi} \int_{-\pi}^{\pi} v^0 \sin n\omega t \, \mathrm{d}\omega t. \tag{8}$$

Harmonic components ($n \ge 2$) do not generate active power with the grid currents, and are not taken into consideration. The Fourier coefficients of the fundamental frequency component are given by

$$\begin{aligned} a_1 = \frac{1}{2\pi} \Big[ &- 8V_p \sin(\beta + \alpha) - \sqrt{2}\pi V^+ \\ &+ \sqrt{6} V^+ \cos 2(\beta + \alpha) - \sqrt{6} V^+ \Big] \end{aligned} \tag{9}$$

$$\begin{aligned} b_1 = \frac{1}{2\pi} \Big[ &8V_p \cos(\beta + \alpha) + \sqrt{6} V^+ \sin 2\beta \\ &- 2\sqrt{6} V^+ (\beta + \alpha) + 3\sqrt{6}\pi V^+ \Big] \end{aligned} \tag{10}$$

where $V^+$ denotes the rms value of the positive sequence component of the converter output voltages. Under the same power imbalance case, the fundamental frequency component of OZSI should be identical to FFZSI in (3) and (4), and therefore

$$\sqrt{2} V^0 = \sqrt{a_1^2 + b_1^2} \tag{11}$$

$$\theta = -\arctan \frac{b_1}{a_1}. \tag{12}$$

To obtain $V_p$ and $\beta$, the transcendental (9)–(12) have to be solved. The fixed point iteration to solve $\beta$ is given by

$$\begin{aligned} \beta_{k+1} &= \varphi(\beta_k), \qquad k = 0, 1, 2 \ldots \\ \varphi(\beta_k) &= -\frac{\sqrt{3} V^0}{3V^+} \cos(\beta_k + \alpha) \cot(\beta_k + \alpha) \\ &\quad - \frac{\sqrt{3}\pi}{6} \cot(\beta_k + \alpha) + \frac{1}{2} \sin 2(\beta_k + \alpha) \\ &\quad + \frac{1}{2} \left(\cos 2(\beta_k + \alpha) - 1\right) \cot(\beta_k + \alpha) \\ &\quad + \frac{\sqrt{3} V^0}{3V^+} \pi \sin(\theta + \alpha) + \frac{3\pi}{2} - \alpha. \end{aligned} \tag{13}$$

The zero-crossing angle (negative to positive) of FFZSI can be given by

$$\gamma = 270^\circ - \theta \tag{14}$$

which can be used as the initial guess for the iteration, because $\gamma$ is very close to $\beta$, as depicted in Fig. 5(d).

Once $\beta$ is solved, $V_p$ can be given by

$$\begin{aligned} V_p = \frac{1}{8 \sin(\beta + \alpha)} \Big[ &\sqrt{6} V^+ \left(\cos 2(\beta + \alpha) - 1\right) \\ &- 2\sqrt{2}\pi V^0 \cos(\theta - \alpha) - \sqrt{2}\pi V^+ \Big]. \end{aligned} \tag{15}$$

A further investigation presented in the Appendix demonstrates that the fixed point iteration method based on (13) may fail to converge in some cases. Therefore, an advanced method, namely Steffensen's method [23], is implemented as follows:

$$\begin{aligned} \beta_{k+1} &= \psi(\beta_k), \qquad k = 0, 1, 2 \ldots \\ \psi(\beta_k) &= \beta_k - \frac{\left(\varphi(\beta_k) - \beta_k\right)^2}{\varphi(\varphi(\beta_k)) - 2\varphi(\beta_k) + \beta_k}. \end{aligned} \tag{16}$$

Steffensen's method ensures iteration convergence. It also achieves quadratic convergence as does Newton–Raphson method, but without using derivatives. The Appendix also shows

TABLE II
PARAMETERS OF THE DESIGNED THREE-PHASE, SEVEN-LEVEL CHB CONVERTER

| Parameters | Values |
|---|---|
| Three-Phase Nominal Power, $P_{\text{nom}}$ | 10 MW |
| Grid Voltage, $V_g$ | 6600 V |
| Capacitor Voltage, $v_{\text{dc}}$ | 2200 V |
| Filtering Inductor, $L_f$ | 5 mH |

a case when Steffensen's method reaches a negligible error ($|\varepsilon| < 0.01\%$) within only two iterations. This rapid convergence property makes it practical for implementation using a low-cost digital signal processor.

The entire period can be divided into six segments, as shown in Fig. 5(d). The above analysis is only carried out for Segment V ($240^\circ - \alpha \leq \beta < 300^\circ - \alpha$), and the calculation of $v^0$ in other segments can be transformed to Segment V, without deriving their own iteration equation.

For $\gamma$ in Segment N (N = I, II,...,VI), a fictitious $\gamma^*$ in Segment V can be created by

$$\gamma^* = \gamma - (N-5)\,\frac{\pi}{3}. \tag{17}$$

Since the fictitious $\gamma^*$ is in Segment V, the iteration equation derived in the manuscript can be used directly to calculate the fictitious $\beta^*$, and then $V_p^*$. Finally, the fictitious $\beta^*$ is transformed back to $\beta$ in Segment N by

$$\beta = \beta^* + (N-5)\,\frac{\pi}{3} \tag{18}$$

and $V_p$ should be equal to $V_p^*$. In this way, $\beta$ and $V_p$ in a segment other than Segment V has been solved without repeating the complicated derivation process.

### C. *Relationship Between $\gamma$ and $\beta$*

A further discussion of the relationship between angles $\gamma$ and $\beta$ is provided to justify the choice of $\gamma$ as the initial guess to solve $\beta$ by iteration (16).

Table II shows the parameters of the three-phase, seven-level CHB converter used as an example. The converter is assumed to operate with an average power generation ratio $\bar{\lambda}$ of 0.8619. The discrepancy between $\gamma$ and $\beta$, plotted with different $v_f^0$ $\left(0.1 \leq V^0/V^+ \leq 0.15, 0 \leq \theta < 360^\circ\right)$, is demonstrated in Fig. 6. The figure shows that $\gamma$ and $\beta$ are close $(<6^\circ)$ in the chosen range. Since the discrepancy decreases with the increase of $V^0/V^+$, for the slight imbalance case $\left(V^0/V^+ < 0.1\right)$, the discrepancy is relatively large. However, the fact is that the slight imbalance can be easily coped with by FFZSI, and there is no need for OZSI. For the severely imbalance case $\left(V^0/V^+ > 0.15\right)$, the discrepancy is very small.

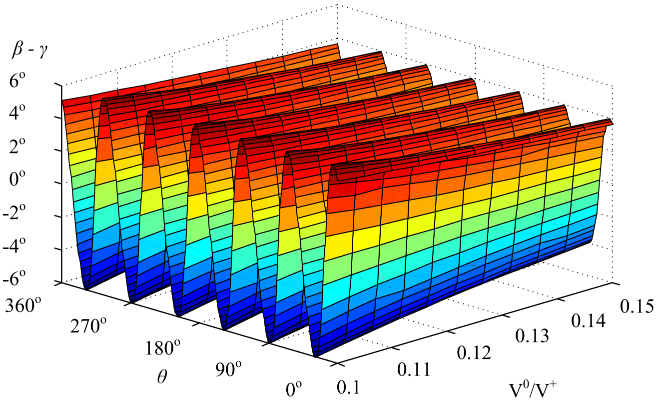

Fig. 6. Discrepancy between $\beta$ and $\gamma$ with different power imbalance cases $\left(0.1 \leq V^0/V^+ \leq 0.15, 0 \leq \theta < 360^\circ\right)$.

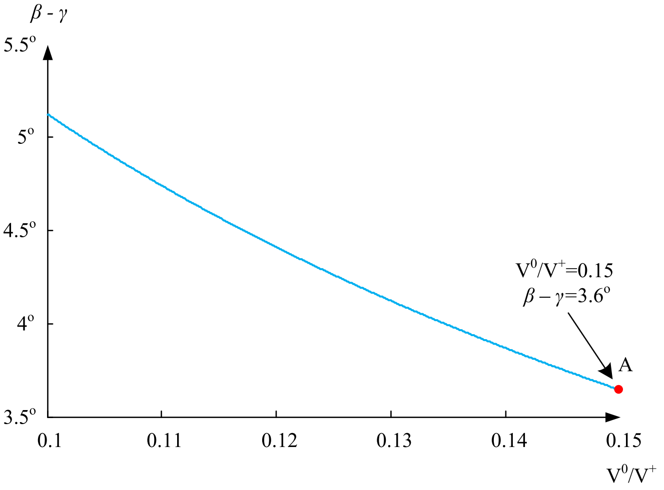

Fig. 7. Relationship between $(\beta - \gamma)$ and $V^0/V^+$ with $\theta = 0^\circ$.

A further investigation presented in Fig. 7 shows that, for a given $\theta$, the angle difference $(\beta - \gamma)$ decreases with the increase of $V^0/V^+$, which means $\gamma$ and $\beta$ become even closer in cases of more severe power imbalance. The relationship between $(\beta - \gamma)$ and $\theta$ is also shown in Fig. 8 for a given $V^0/V^+$. The angle difference oscillates six cycles each fundamental period, corresponding to the six segments in Fig. 5(d). $\beta$ equals $\gamma$ at segment start/end points

$$\beta = \gamma = N \cdot 60^\circ - \alpha, \quad N = 1, 2, \ldots, 6 \tag{19}$$

and middle points

$$\beta = \gamma = N \cdot 60^\circ - 30^\circ - \alpha, \quad N = 1, 2, \ldots, 6. \tag{20}$$

On these occasions, the voltage overhead is naturally quarter-wave (QW) symmetrical, as shown in Fig. 9. As a result, the voltage overhead and its fundamental frequency share the same zero-crossing point. It can be further observed that $\gamma$ and $\beta$ are always in the same segment, because the slopes at the interval points in Fig. 8 are less than unity. This characteristic validates the separate derivation of $\beta$ for the six segments.

## IV. SOZSI

### A. *Derivation of the Simplified Method*

Both Steffensen's method and the choice of $\gamma$ as the initial guess for $\beta$ contribute to the fast convergence of the iteration.

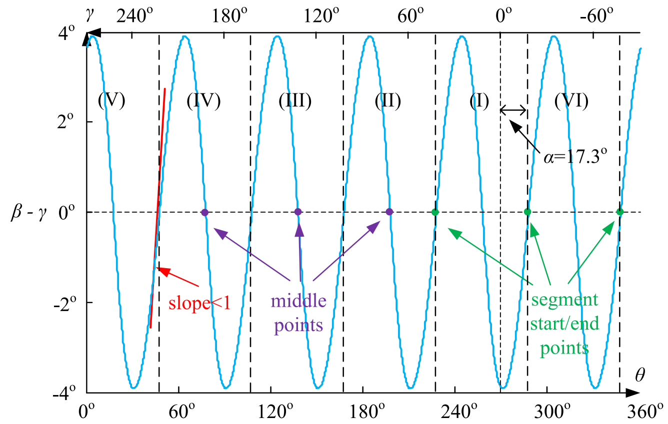

Fig. 8. Relationship between $(\beta - \gamma)$ and $\theta$ with $V^0/V^+ = 0.15$.

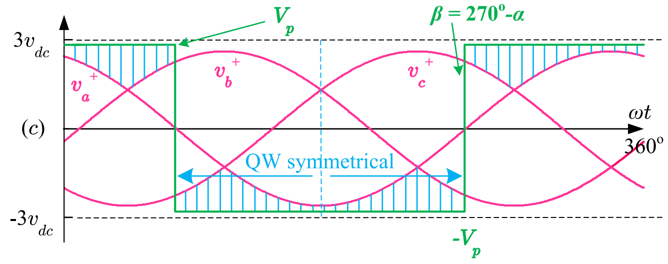

Fig. 9. Naturally quarterly-wave symmetrical voltage overhead $(\beta = 270^\circ - \alpha)$.

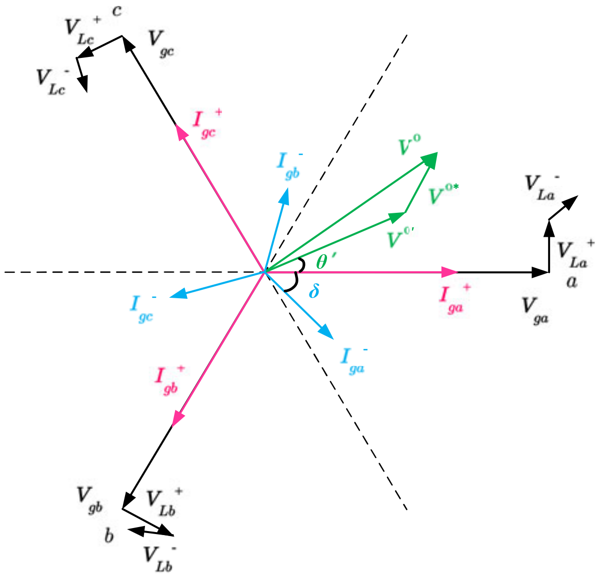

Fig. 10. Phasor diagram with inaccurate zero sequence injection and negative sequence grid currents.

Since $\beta$ and $\gamma$ are close (see Section III), a simplified method can be achieved by directly using $\gamma$ as an approximation of $\beta$, thus avoiding the numerical iteration. The corresponding peak voltage of the simplified method can be derived by substituting $\gamma$ for $\beta$ in (15)

$$V_p' = \frac{1}{8\sin(\gamma+\alpha)}\left[\sqrt{6}V^+\left(\cos 2(\gamma+\alpha) - 1\right) - 2\sqrt{2}\pi V^0 \cos(\theta-\alpha) - \sqrt{2}\pi V^+\right]. \tag{21}$$

## B. Error Estimation

Compared to OZSI, SOZSI features simpler implementation by avoiding solution of the transcendental (9)–(12). However, negative sequence grid currents occur as a result of the inaccurate zero sequence injection with the approximation of (21).

As shown in Fig. 10, the fundamental frequency zero sequence vector of SOZI $\mathbf{V}^{0'}$ deviates from that of OZSI $\mathbf{V}^0$ by an error vector $\mathbf{V}^{0*}$, which undermines the power redistribution among the three phases by the zero sequence injection. For example, in Fig. 10 less power is delivered to the grid by phase $a$, whereas the PV power generation remains unchanged. The negative sequence grid current vectors $\mathbf{I}_{\mathrm{ga}}^-$, $\mathbf{I}_{\mathrm{gb}}^-$ and $\mathbf{I}_{\mathrm{gc}}^-$ are thus generated to balance the input and output powers of the dc-side capacitors

$$\mathbf{V}^{0*} \cdot \mathbf{I}_{\mathrm{ga}}^+ = \mathbf{V}_{\mathrm{ga}} \cdot \mathbf{I}_{\mathrm{ga}}^- + \mathbf{V}^{0'} \cdot \mathbf{I}_{\mathrm{ga}}^- + \mathbf{V}_{\mathrm{La}}^+ \cdot \mathbf{I}_{\mathrm{ga}}^- + \mathbf{V}_{\mathrm{La}}^- \cdot \mathbf{I}_{\mathrm{ga}}^+ \tag{22}$$

$$\mathbf{V}^{0*} \cdot \mathbf{I}_{\mathrm{gb}}^+ = \mathbf{V}_{\mathrm{gb}} \cdot \mathbf{I}_{\mathrm{gb}}^- + \mathbf{V}^{0'} \cdot \mathbf{I}_{\mathrm{gb}}^- + \mathbf{V}_{\mathrm{Lb}}^+ \cdot \mathbf{I}_{\mathrm{gb}}^- + \mathbf{V}_{\mathrm{Lb}}^- \cdot \mathbf{I}_{\mathrm{gb}}^+ \tag{23}$$

$$\mathbf{V}^{0*} \cdot \mathbf{I}_{\mathrm{gc}}^+ = \mathbf{V}_{\mathrm{gc}} \cdot \mathbf{I}_{\mathrm{gc}}^- + \mathbf{V}^{0'} \cdot \mathbf{I}_{\mathrm{gc}}^- + \mathbf{V}_{\mathrm{Lc}}^+ \cdot \mathbf{I}_{\mathrm{gc}}^- + \mathbf{V}_{\mathrm{Lc}}^- \cdot \mathbf{I}_{\mathrm{gc}}^+. \tag{24}$$

The amplitude $I_g^-$ and phase angle $-\delta$ of the negative sequence grid current vectors can thus be solved analytically.

The current imbalance can be described by the imbalance factor $\eta$ defined in [24] as

$$\eta = \frac{I_g^-}{I_g^+}. \tag{25}$$

The amplitude of the negative sequence grid currents $I_g^-$ should be much smaller compared to that of the positive sequence grid currents $I_g^+$. Vectors $\mathbf{I}_{\mathrm{ga}}^-$, $\mathbf{I}_{\mathrm{gb}}^-$, $\mathbf{I}_{\mathrm{gc}}^-$ and $\mathbf{V}_{\mathrm{La}}^-$, $\mathbf{V}_{\mathrm{Lb}}^-$, $\mathbf{V}_{\mathrm{Lc}}^-$ are therefore exaggerated in Fig. 10 to enable clear demonstration. Excessive injection of negative sequence currents into the grid is forbidden by most grid codes [25], because they contribute to supply voltage imbalance.

The imbalance factor $\eta$ due to the approximation of (21) is plotted in Fig. 11, with an average power generation ratio $\bar{\lambda}$ of 0.8619 $\left(0.1 \le V^0/V^+ \le 0.15, 0 \le \theta < 360^\circ\right)$. The converter parameters used are listed in Table II. It is observed that $\eta$ is negligibly small ($< 1.2\%$) for the case under study.

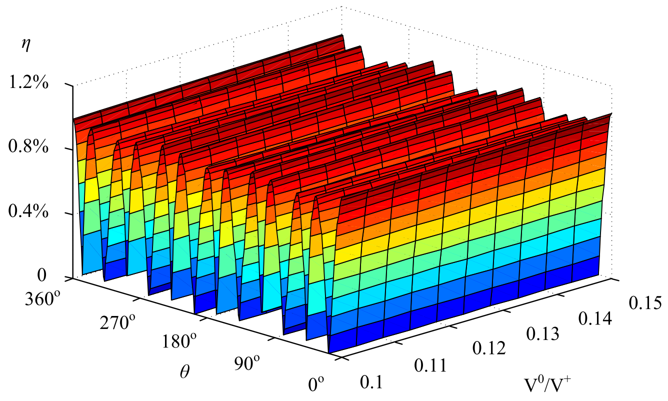

Fig. 11. Imbalance factor $\eta$ of SOZSI with different power imbalance cases $\left(0.1 \leq V^0/V^+ \leq 0.15, 0 \leq \theta < 360°\right)$.

TABLE III
PV PARAMETERS

| Parameters | Values |
|---|---|
| PV Module Type | BP 365 |
| Output Voltage at Maximum Power Point | 17.65 V |
| Output Current at Maximum Power Point | 3.68 A |
| Maximum Power | 65 W |
| Cascaded PV Modules per String | 55 |
| Paralleled Strings per H-Bridge | 311 |

## V. SIMULATION RESULTS

The parameters of the simulated three-phase, seven-level CHB converter are listed in Table II. The capacitor voltage of each H-bridge was regulated to be constant at 2200 V with a capacitance value of 10 mF. With three series bridges in each phase, the converter is able to connect to the 6.6 kV distribution network directly, without a line-frequency power transformer. In real applications the capacitor voltage could be lower if more H-bridges were introduced. The multilevel waveform synthesis allows the switching frequency to be as low as 600 Hz, thus greatly reducing the switching loss. An individual PV module (BP365) reaches a nominal peak power output of 65 W at 1000 W/m$^2$ and 25 °C. Each H-bridge is fed by 55 × 311 modules with a total nominal peak output power of 1.11 MW (see Table III).

The dc-side capacitor voltages $v_{\mathrm{dc}}$ of the CHB converter are regulated by the VOC [see Fig. 12(a)]. The zero sequence $v^0$, which is the focus of this paper, was generated based on the three-phase power generation ratios $\lambda_a$, $\lambda_b$ and $\lambda_c$ by FFZSI, OZSI or SOZSI. The converter output voltage references $v_a$, $v_b$ and $v_c$ were finally obtained by adding $v^0$ to the positive sequence component $v_a^+$, $v_b^+$ and $v_c^+$.

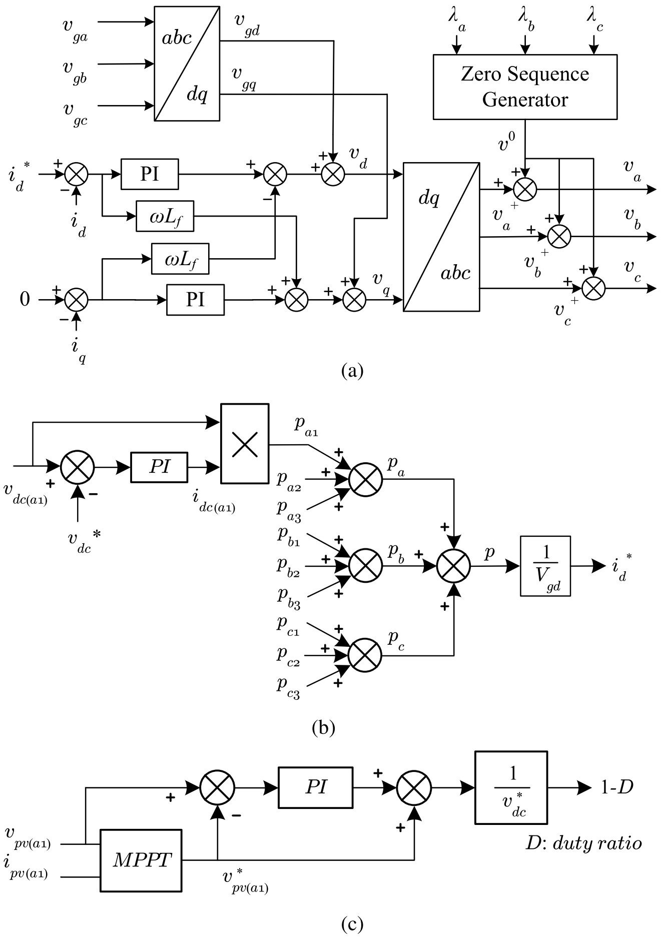

Fig. 12. Control implementation. (a) VOC of the CHB converter; (b) obtaining the power references; (c) regulation of the dc–dc converter.

The power reference of each bridge $p_{ij}$ $(i = a, b, c, j = 1, 2, 3)$ is obtained by comparing the measured capacitor voltage $v_{\mathrm{dc}(ij)}$ $(i = a, b, c, j = 1, 2, 3)$ with the command reference $v_{\mathrm{dc}}^*$ [see Fig. 12(b)]. In this paper, $v_{\mathrm{dc}}^*$ is equal for each bridge and remains constant despite of the power variation. Hence, a standard multilevel waveform with an equal and constant voltage step can be achieved. The three-phase overall power reference $p$ is obtained by summing the power references of the nine bridges $\sum_{i=a}^{c}\sum_{j=1}^{3} v_{\mathrm{dc}(ij)}$. Similarly, the phase power references $p_i$ $(i = a, b, c)$ are obtained by summing the power references of the three bridge in the phase $\sum_{j=1}^{3} v_{\mathrm{dc}(ij)}$ $(i = a, b, c)$, and the power generation ratios $\lambda_a, \lambda_b, \lambda_c$ can be calculated (1).

The regulation of the dc–dc converter [see Fig. 12(c)] is decoupled from the VOC of the CHB converter, because the dc-side capacitor voltages $v_{\mathrm{dc}}$ are constant. By regulating the PV output voltage $v_{\mathrm{pv}}$ to the command reference $v_{\mathrm{pv}}^*$, the dc–dc converter tracks the maximum power point of the PV array.

### A. *Case I* $(\lambda_a = 1, \lambda_b = 0.7929, \lambda_c = 0.7929)$

It was assumed that the irradiance of the PV modules of phases $b$ and $c$ decreases from 1000 to 800 W/m$^2$, corresponding to 79.29% of their nominal power, whereas the irradiance of phase $a$ remains at 1000 W/m$^2$. This case corresponds to Point A $(V^0/V^+ = 0.15, \theta = 0°)$ in Fig. 7 with an angle difference $\beta - \gamma$ of 3.6°.

In this case, three-phase balanced grid currents can be provided with FFZSI as well as OZSI and SOZSI (see Fig. 13). The converter output voltages feature seven-level waveforms as expected, and the measured grid currents imbalance and harmonic distortion are listed in Table IV.

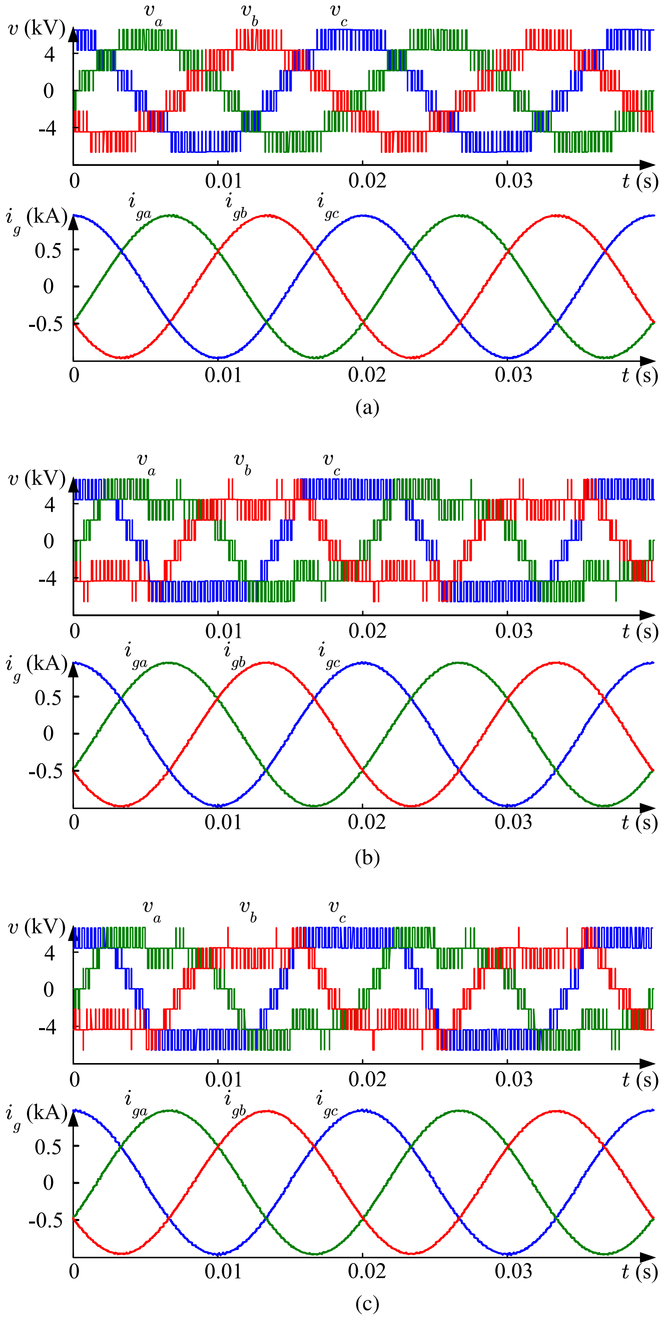

Fig. 13. Simulation results of converter output voltages $v_a$, $v_b$, $v_c$ and grid currents $i_{ga}$, $i_{gb}$, $i_{gc}$ of unbalanced operation Case I with (a) FFZSI, (b) OZSI, (c) SOZSI.

TABLE IV
CURRENT IMBALANCE AND DISTORTION (CASE I)

| Methods | Imbalance Ratio $\eta$ | Distortion | | |
|---|---|---|---|---|
| | | THD $(i_{ga})$ | THD $(i_{gb})$ | THD $(i_{gc})$ |
| FFZSI | 0.03% | 0.56% | 0.66% | 0.68% |
| OZSI | 0.02% | 0.86% | 0.70% | 0.66% |
| SOZSI | 1.03% | 0.87% | 0.74% | 0.72% |

The converter output voltage waveforms of OZSI and SOZSI illustrate that the power devices continue to switch on and off as usual, and no significant harmonic increase can be observed, which differentiates the proposed methods from discontinuous modulation.

### B. *Case II* $(\lambda_a = 1, \lambda_b = 0.5862, \lambda_c = 0.5862)$

In this case, it was assumed that the irradiance of the PV modules of phases $b$ and $c$ falls further from 800 to 600 W/m$^2$, corresponding to 58.62% of their nominal power, whereas the irradiance of phase $a$ remains at 1000 W/m$^2$.

The grid currents and converter output voltages with the conventional FFZSI are shown in Fig. 14(a), where obvious imbalance and harmonic distortion can be observed. The converter fails to provide balanced grid currents to meet the grid code, because this power imbalance case is beyond the capability of FFZSI. However, OZSI and SOZSI, shown in Fig. 14(b) and (c), respectively, are able to deal with the power imbalance. Both OZSI and SOZSI make best use of the available dc-side capacitor voltage to avoid converter saturation. Three-phase balanced grid currents are thus guaranteed.

The results in Tables IV and V show that SOZSI generates a higher imbalance ratio than OZSI, as expected. Therefore, use of the simplified method is limited to applications where a small amount of negative sequence can be tolerated.

## VI. EXPERIMENTAL RESULTS

Fig. 15 shows the 9-kW three-phase, seven-level CHB converter designed, constructed and tested in the laboratory to verify the effectiveness of the presented methods.

The prototype was fed by nine isolated Ametek Elgar TerraSAS PV simulators, each rated at 600 V and 8 A and loaded with the characteristic profile of the GE PVp-200-M (54 cells) PV module. In this experiment, each simulator was programmed to imitate the output characteristics of a string with five PV modules in series. A nominal peak power output of 1002.85 W (134.75 V and 7.442 A) was thus expected for each bridge at 1000 W/m$^2$ and 25 °C. With a total of nine bridges, the converter delivers a nominal power of 9 kW into the grid. Nine APS Powerex IGBT H-bridge modules (PP75B060) rated at 600 V and 75 A were used to construct the three-phase seven-level converter.

The capacitor voltage was fixed at 135 V, which tracks the maximum power point at 1000 W/m$^2$ and 25 °C. The dc–dc conversion stage, which is necessary in field applications, is not included in the setup. The CHB converter is still regulated by VOC, and $v_{\mathrm{dc}}$ remains constant. Without dc–dc converters, the variation of the maximum power point, owing to irradiance or temperature changes, cannot be always tracked. However, this does not affect the purpose of this paper, which is to demonstrate zero sequence injection methods, as long as the interphase power imbalance is created. Each module comes with electrolytic capacitors with a capacitance value of 18 mF, which corresponds to a unit capacitance constant $H$ of 164 ms at 135 V [26].

The control strategy was implemented in a dSPACE DS1006 platform with onboard Xilinx FPGA modules operating at 100 MHz to ensure real time PWM generation. The carrier

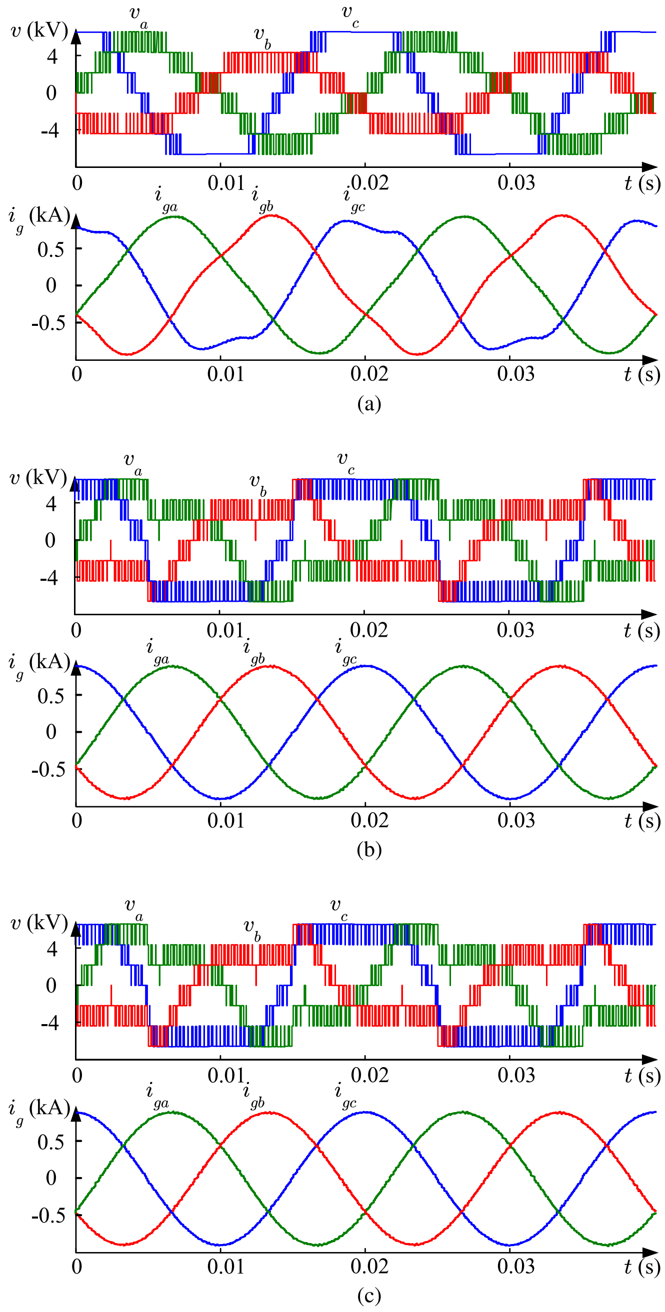

Fig. 14. Simulation results of converter output voltages $v_a$, $v_b$, $v_c$ and grid currents $i_{ga}, i_{gb}, i_{gc}$ of unbalanced operation Case II with (a) FFZSI, (b) OZSI, (c) SOZSI.

TABLE V
CURRENT IMBALANCE AND DISTORTION (CASE II)

| Methods | Imbalance Ratio $\eta$ | Distortion | | |
|---|---|---|---|---|
| | | THD $(i_{ga})$ | THD $(i_{gb})$ | THD $(i_{gc})$ |
| FFZSI | N/A | 12.33% | 5.01% | 8.78% |
| OZSI | 0.05% | 1.07% | 0.94% | 0.91% |
| SOZSI | 0.70% | 0.76% | 0.90% | 0.94% |

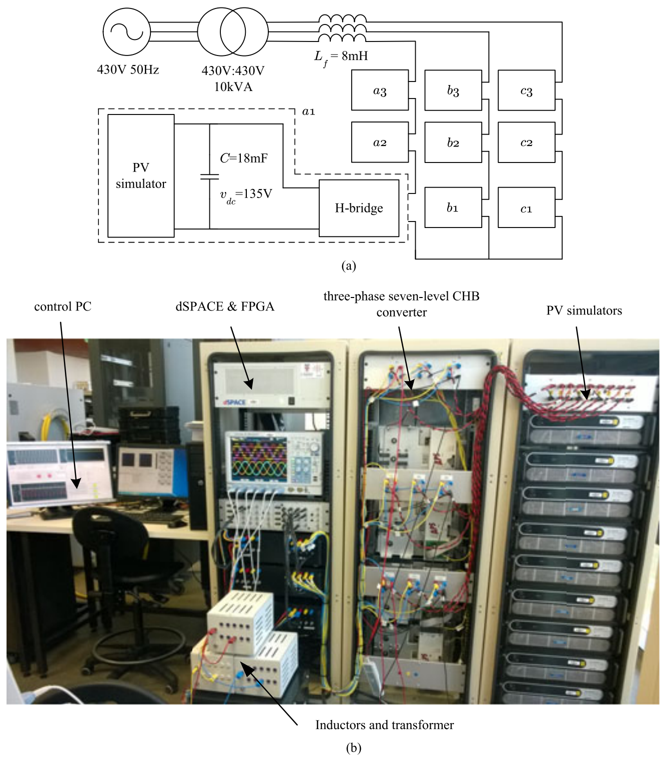

Fig. 15. Experimental setup: (a) schematic diagram and (b) hardware image.

frequency of the phase-shifted (PS) PWM was chosen to be 600 Hz, representing a switching frequency practical for real applications. Since three H-bridges are cascaded in one phase leg, the converter output phase voltages feature seven-level waveforms with an equivalent switching frequency of 3.6 kHz. Finally, the prototype was connected to the 430-V three-phase utility grid via three-phase filtering inductors (8 mH per phase).

Fig. 16(a) shows the experimental results under balanced power generation when all PV strings are subject to 1000 W/m$^2$ and 25 °C. The converter output voltages feature seven-level synthesized waveforms as expected, and grid currents are symmetrical with limited harmonics.

The solar irradiance level was decreased from 1000 to 700 W/m$^2$ in phase $a$, corresponding to approximately 70% of its peak power. The irradiance levels in the simulators of phases $b$ and $c$ remained at 1000 W/m$^2$. Fig. 16(b) shows the results with FFZSI. Three-phase grid currents are unbalanced and distorted, because the power imbalance is beyond the balance capability of the converter and saturation occurs. However, the proposed OZSI and SOZSI are still able to provide three-phase balanced grid currents, as shown in Fig. 17. The superior power balance performance of the presented methods is thus confirmed. A ramp response from $(\lambda_a = 1, \lambda_b = 1, \lambda_c = 1)$ to $(\lambda_a \approx 0.7, \lambda_b \approx 0.8, \lambda_c \approx 0.8)$ (ramp time $t = 1$ s) is shown in Fig. 18, which confirms the dynamic performance of the proposed OZSI.

Table VI summarizes the grid current imbalance ratios with different methods. It can be seen that under balanced power generation, the converter injects negative sequence currents into the grid, with an amplitude of 0.82% of the amplitude of the positive sequence currents. This can be explained by the fact

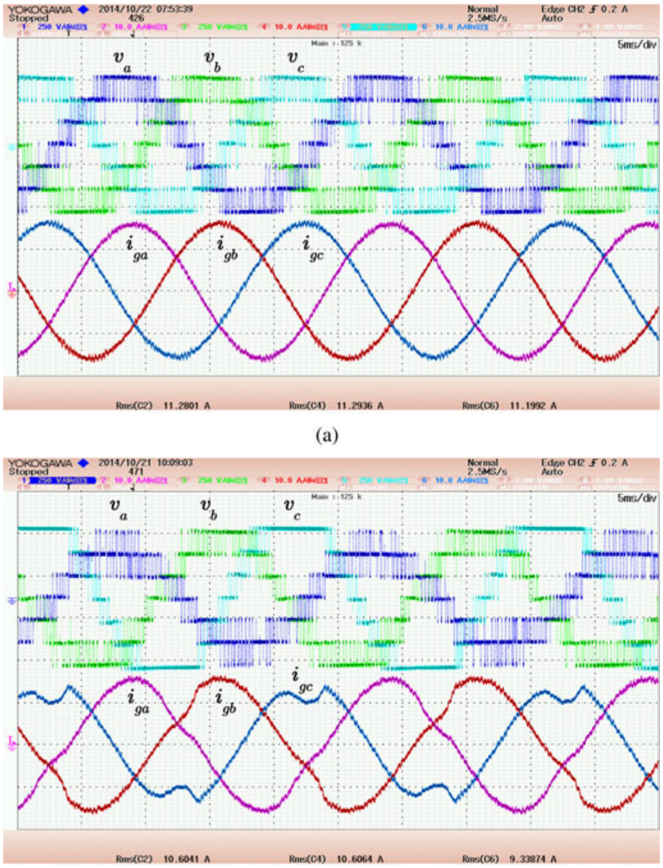

(a)

(b)

Fig. 16. Experimental results of converter output voltages and grid currents of (a) balanced operation, (b) unbalanced operation with FFZSI. CH1: converter output voltage of phase $a$ $v_a$; CH2: grid current of phase $a$ $i_{ga}$; CH3: converter output voltage of phase $b$ $v_b$; CH4: grid current of phase $b$ $i_{gb}$; CH5: converter output voltage of phase $c$ $v_c$; CH6: grid current of phase $c$ $i_{gc}$. CH1, CH3, CH5: 250 V/div; CH2, CH4, CH6: 10 A/div.

that the 430 V power grid in the authors' laboratory is not ideal, with an imbalance ratio of 0.16%. The inductance asymmetry of three-phase inductors and other imperfect devices may also contribute to the increase of negative sequence currents. The simplified method features a slightly higher imbalance ratio, because of the approximation made in the derivation, which agrees well with the simulation results.

The zero sequence injections of FFZSI, OZSI and SOZSI are demonstrated in Fig. 19. It once more confirms that all three methods share the identical fundamental frequency component, which is crucial to the interphase power balance.

## VII. CONCLUSION

Injection of a zero sequence into the converter output voltages is necessary in order to deal with interphase power imbalance in CHB PV converters. An OZSI proposed in this paper extends the power balance range of the converter by making full use of the available voltage overhead. As a result, three-phase balanced grid currents can be guaranteed even with severe power imbalance. A SOZSI has also been developed. It reduces the calculation effort at the cost of additional negative sequence grid currents, owing to the injection of an inaccurate zero sequence introduced by the approximation. The amount of negative sequence currents with SOZSI is limited, while the iteration with OZSI features very rapid convergence. Simulation and experimental results from a three-phase seven-level laboratory prototype have been provided to validate the feasibility of the proposed methods.

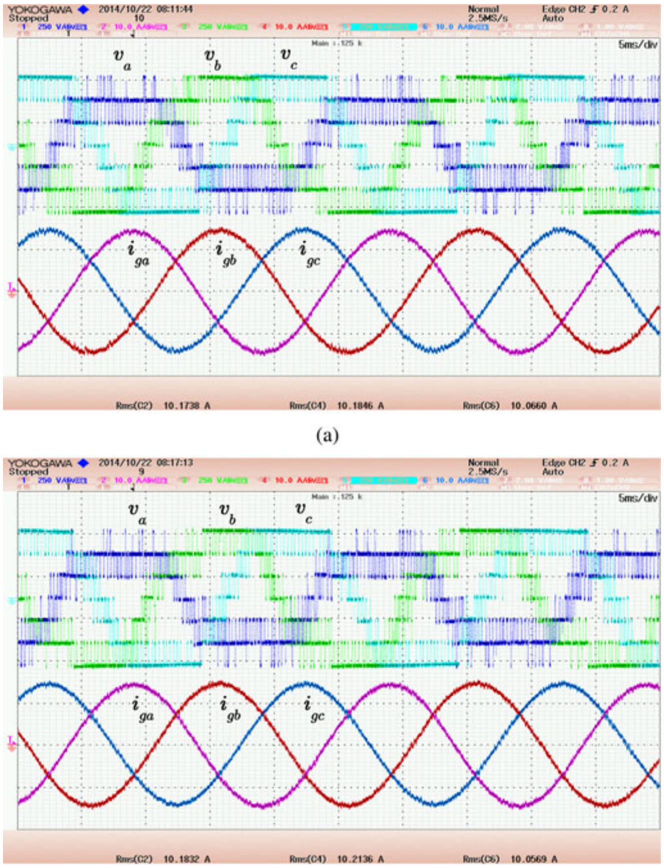

(a)

(b)

Fig. 17. Experimental results of converter output voltages and grid currents of unbalanced operation with (a) OZSI, (b) SOZSI. CH1: converter output voltage of phase $a$ $v_a$; CH2: grid current of phase $a$ $i_{ga}$; CH3: converter output voltage of phase $b$ $v_b$; CH4: grid current of phase $b$ $i_{gb}$; CH5: converter output voltage of phase $c$ $v_c$; CH6: grid current of phase $c$ $i_{gc}$. CH1, CH3, CH5: 250 V/div; CH2, CH4, CH6: 10 A/div.

## APPENDIX

This Appendix is devoted to the comparison of two numerical methods: the fixed point iteration and Steffensen's method, demonstrating the necessity of introducing Steffensen's method and its rapid convergence. The parameters of the analyzed converter are listed in Table II. It is assumed that both phases $b$ and $c$ generate 79.29% of the single-phase nominal power, whereas phase $a$ produces full power (the same as simulation Case I)

$$\lambda_a = 1 \quad \lambda_b = 0.7929 \quad \lambda_c = 0.7929. \tag{26}$$

Based on the operation point, other parameters can be calculated and are listed in Table VII. $\gamma$ is used as the initial value to

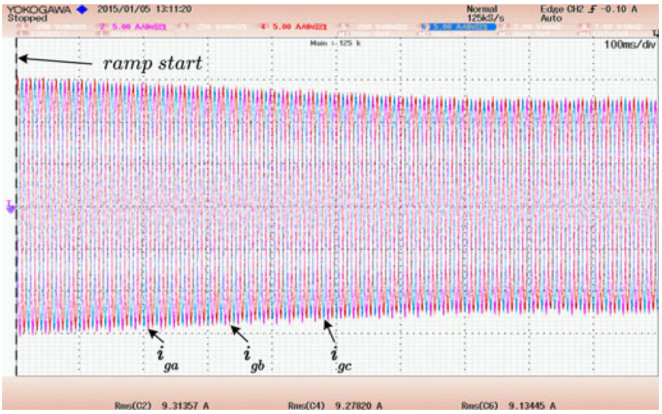

Fig. 18. Dynamic performance of grid currents of unbalanced operation with OZSI. CH2: grid current of phase $a$ $i_{ga}$; CH4: grid current of phase $b$ $i_{gb}$; CH6: grid current of phase $c$ $i_{gc}$. CH2, CH4, CH6: 10 A/div.

TABLE VI
CURRENT IMBALANCE AND DISTORTION (EXPERIMENT)

| Operation | Methods | Imbalance Ratio $\eta$ | Distortion | | |
|---|---|---|---|---|---|
| | | | THD ($i_{ga}$) | THD ($i_{gb}$) | THD ($i_{gc}$) |
| Balanced | N/A | 0.82% | 0.86% | 0.85% | 0.83% |
| Unbalanced | OZSI | 0.83% | 0.97% | 0.94% | 0.91% |
| | SOZSI | 1.00% | 0.99% | 1.02% | 0.89% |

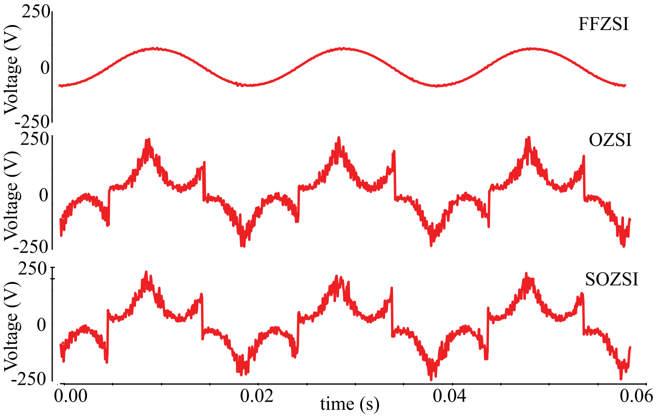

Fig. 19. Experimentally measured zero sequence injections of FFZSI, OZSI and SOZSI.

solve $\beta$ by iteration. Results based on fixed point iteration and Steffensen's method are compared in Table VIII. These results demonstrate that fixed point iteration results in a value lying outside Segment V under discussion [see Fig. 5(d)], after 12 iterations

$$\beta_{12} = 218.8182^\circ < 240^\circ - \alpha = 222.7^\circ \tag{27}$$

and it fails to converge. Steffensen's method, however, ensures the convergence and is able to reach a negligible error ($|\varepsilon| < 0.01\%$) with two iterations.

TABLE VII
OTHER CONVERTER PARAMETERS

| Parameters | $I_g$ | $V^+$ | $V^0$ | $\alpha$ | $\theta$ | $\gamma$ |
|---|---|---|---|---|---|---|
| Values | 754 A | 3990 V | 610 V | 17.3° | 0° | 270° |

TABLE VIII
COMPARISON OF THE FIXED POINT ITERATION AND STEFFENSEN'S METHOD

| Iteration Times | $\beta$ | Fixed Point Iteration | Steffensen's Method |
|---|---|---|---|
| Initialization | $\gamma$ | $270.0000^\circ$ | $270.0000^\circ$ |
| 1 | $\beta_1$ | $268.8842^\circ$ | $274.0151^\circ$ |
| 2 | $\beta_2$ | $267.4584^\circ$ | $273.5758^\circ$ |
| 3 | $\beta_3$ | $265.6594^\circ$ | $273.5688^\circ$ |
| 4 | $\beta_4$ | $263.4229^\circ$ | $273.5688^\circ$ |
| ⋮ | ⋮ | ⋮ | ⋮ |
| 12 | $\beta_{12}$ | $218.8182^\circ$ | $273.5688^\circ$ |

## REFERENCES

[1] S. Kouro, M. Malinowski, K. Gopakumar, J. Pou, L.G. Franquelo, B. Wu, J. Rodriguez, M. A. Perez, and J. I. Leon, "Recent advances and industrial applications of multilevel converters," *IEEE Trans. Ind. Electron.*, vol. 57, no. 8, pp. 2553–2580, Aug. 2010.

[2] M. Malinowski, K. Gopakumar, J. Rodriguez, and M. A. perez, "A survey on cascaded multilevel inverters," *IEEE Trans. Ind. Electron.*, vol. 57, no. 7, pp. 2197–2206, Jul. 2010.

[3] H. Abu-Rub, J. Holtz, J. Rodriguez, and B. Ge, "Medium-voltage multilevel converters: State of the art, challenges, and requirements in industrial applications," *IEEE Trans. Ind. Electron.*, vol. 57, no. 8, pp. 2581–2596, Aug. 2010.

[4] S Rohner, S Bernet, M. Hiller, and R. Sommer, "Modulation, losses, and semiconductor requirements of modular multilevel converters," *IEEE Trans. Ind. Electron.*, vol. 57, no. 8, pp. 2633–2642, Aug. 2010.

[5] J. Carrasco, L. Franquelo, J. Bialasiewicz, E. Galvan, R. Guisado, M. Prats, J. Leon, and N. Alfonso, "Power-electronic systems for the grid integration of renewable energy sources: A survey," *IEEE Trans. Ind. Electron.*, vol. 53, no. 4, pp. 1002–1016, Jun. 2006.

[6] P. Lezana, J. Pou, T. A. Meynard, J. Rodriguez, S. Ceballos, and F. Richardeau, "Survey on fault operation on multilevel inverters," *IEEE Trans. Ind. Electron.*, vol. 57, no. 7, pp. 2207–2218, Jul. 2010.

[7] M. Cavalcanti, A. Farias, K. Oliveira, and J. Afonso, "Eliminating leakage currents in neutral point clamped converters for photovoltaic systems," *IEEE Trans. Ind. Electron.*, vol. 59, no. 1, pp. 435–443, Jan. 2012.

[8] S. Monge, J. Rocabert, P. Rodriguez, S. Alepuz, and J. Bordonau, "Multilevel diode-clamped converter for photovoltaic generators with independent voltage control of each solar array," *IEEE Trans. Ind. Electron.*, vol. 55, no. 7, pp. 2713–2723, Jul. 2008.

[9] M. R. Islam, Y. Guo, and J. Zhu, "A multilevel medium-voltage inverter for step-up-transformer-less grid connection of photovoltaic power plants," *IEEE J. Photovolt.*, vol. 4, no. 3, pp. 881–889, May 2014.

[10] J. Sastry, P. Bakas, H. Kim, L. Wang, and A. Marinopoulos, "Evaluation of cascaded H-bridge inverter for utility-scale photovoltaic systems," *Renewable Energy*, Vol. 69, pp. 208–218, Sep. 2014.

[11] S. Essakiappan, H. S. Krishnamoorthy, P. Enjeti, R. S. Balog, and S. Ahmed, "Multilevel medium frequency link inverter for utility scale photovoltaic integration," *IEEE Trans. Power Electron.*, vol. 30, no. 7, pp. 3674–3684, Jul. 2015.

[12] W. Zhao, H. Choi, G. Konstantinou, M. Ciobotaru, and V. Agelidis, "Cascaded H-bridge multilevel converter for large-scale PV grid-integration with isolated DC-DC stage," in *Proc. IEEE Power Electron. Distrib. Generation Syst.*, 2012, pp. 849–856.

[13] E. Villanueva, P. Correa, J. Rodriguez, and M. Pacas, "Control of a single-phase cascaded H-bridge multilevel converter for grid-connected photovoltaic systems," *IEEE Trans. Ind. Electron.*, vol. 56, no. 11, pp. 4399–4406, Nov. 2009.

[14] J. Chavarria, D. Biel, F. Guinjoan, C. Meza, and J. Negroni, "Energy-balance control of PV cascaded multilevel grid-connected converters under

level-shifted and phase-shifted PWMs," *IEEE Trans. Ind. Electron.*, vol. 60, no. 1, pp. 98–111, Jan. 2013.

[15] C. Townsend, T. Summers, and R. Betz, "Control and modulation scheme for a cascaded H-bridge multi-level converter in large scale photovoltaic systems," in *Proc. IEEE Energy Convers. Congr. Expo.*, 2012, pp. 3707–3714.

[16] Y. Yu, G. Konstantinou, B. Hredzak, and V. Agelidis, "On extending the energy balancing limit of multilevel cascaded H-bridge converters for large-scale photovoltaic farms," in *Proc. Australasian Univ. Power Eng. Conf.*, 2013, pp. 1–6.

[17] S. Rivera, B. Wu, S. Kouro, and D. Zhang, "Cascaded H-bridge multilevel converter topology and three-phase balance control for large scale photovoltaic systems," in *Proc. IEEE Power Electron. Distrib. Generation Syst.*, 2012, pp. 690–697.

[18] B. Xiao, L. Hang, J. Mei, C. Riley, L. Tolbert, and B. Ozpineci, "Modular cascaded H-bridge multilevel PV inverter with distributed MPPT for grid-connected applications," *IEEE Trans. Ind. Appl.*, 2014.

[19] L. Liu, H. Li, Y. Xue, and W. Liu, "Reactive power compensation and optimization strategy for grid-interactive cascaded photovoltaic systems," *IEEE Trans. Power Electron.*, vol. 30, no. 1, pp. 188–202, Jan. 2015.

[20] L. Liu, H. Li, S. Hwang, and J. Kim, "An energy-efficient motor drive with autonomous power regenerative control system based on cascaded multilevel inverters and segmented energy storage," *IEEE Trans. Ind. Appl.*, vol. 49, no. 1, pp. 178–188, Jan./Feb. 2013.

[21] *Thin-Film Terrestrial Photovoltaic (PV) Modules—Design Qualification and Type Approval*, IEC 61646, 2008.

[22] Y. Yu, G. Konstantinou, B. Hredzak, and V. Agelidis, "Optimal zero sequence injection in multilevel cascaded H-bridge converter under unbalanced photovoltaic power generation," in *Proc. IEEE Int. Power Electron. Conf.*, 2014, pp. 1458–1465.

[23] G. Dahlquist and Å. Björck, *Numerical Methods*. Englewood Cliffs, NJ, USA: Prentice-Hall, 1974, pp. 230–232.

[24] *IEEE Recommended Practice for Monitoring Electric Power Quality*, IEEE Standard 1159–2009, 2009.

[25] *IEEE Standard for Interconnecting Distributed Resources With Electric Power Systems*, IEEE Standard 1547, 2003.

[26] H. Akagi, S. Inoue, and T. Yoshii, "Control and performance of a transformerless cascade PWM STATCOM with star configuration," *IEEE Trans. Ind. Appl.*, vol. 43, no. 4, pp. 1041–1049, Jul./Aug. 2007.

**Yifan Yu** (S'13) received the B.Eng. and M.Eng. degrees in electrical engineering from the Harbin Institute of Technology, Harbin, China, in 2010 and 2012, respectively. He is currently working toward the Ph.D. degree at the University of New South Wales, Sydney, Australia.

His research interests include multilevel converters, Z-source inverters, photovoltaic grid connection, and other aspects of power electronic technology for renewable energy sources.

**Georgios Konstantinou** (S'08–M'13) received the B.Eng. degree in electrical and computer engineering from the Aristotle University of Thessaloniki, Thessaloniki, Greece, in 2007, and the Ph.D. degree in electrical engineering from the University of New South Wales (UNSW), Sydney, Australia, in 2012.

He is currently a Senior Research Associate with the Australian Energy Research Institute and the School of Electrical Engineering and Telecommunications, UNSW. He is an Associate Editor of *IET Power Electronics*. His research interests include hybrid and modular multilevel converters, pulse width modulation, and selective harmonic elimination techniques for power electronics.

**Branislav Hredzak** (M'98–SM'13) received the B.Sc. and M.Sc. degrees from the Technical University of Kosice, Kosice, Slovakia, in 1993, and the Ph.D. degree from the Napier University of Edinburgh, Edinburgh, U.K., in 1997, all in electrical engineering.

He was a Lecturer and a Senior Researcher in Singapore from 1997 to 2007. He is currently a Senior Lecturer at the School of Electrical Engineering and Telecommunications, University of New South Wales, Sydney, Australia. His current research interests include hybrid storage technologies and advanced control systems for power electronics and storage systems.

**Vassilios G. Agelidis** (S'89–M'91–SM'00) was born in Serres, Greece. He received the B.Eng. degree in electrical engineering from the Democritus University of Thrace, Thrace, Greece, in 1988, the M.S. degree in applied science from Concordia University, Montreal, Canada, in 1992, and the Ph.D. degree in electrical engineering from Curtin University, Perth, Australia, in 1997.

He was with Curtin University (1993–1999), the University of Glasgow, Glasgow, U.K. (2000–2004), Murdoch University, Perth, Australia (2005–2006), and the University of Sydney, Sydney, Australia (2007–2010). He is currently the Director of the Australian Energy Research Institute, School of Electrical Engineering and Telecommunications, University of New South Wales, Sydney.

Dr. Agelidis received the Advanced Research Fellowship from the U.K. Engineering and Physical Sciences Research Council in 2004. He was the Vice President for operations with the IEEE Power Electronics Society (PELS) from 2006 to 2007. He was an AdCom Member of the IEEE PELS from 2007 to 2009 and the Technical Chair of the IEEE Power Electronics Specialists Conference in 2008 held in Rhodes, Greece.